View Online

Mechanics of curvilinear electronics†

Shuodao Wang,[a] Jianliang Xiao,[b] Jizhou Song,[c] Heung Cho Ko,[d] Keh-Chih Hwang,[e] Yonggang Huang*[af] and John A. Rogers*[bg]

Received 25th June 2010, Accepted 10th September 2010
DOI: 10.1039/c0sm00579g

Advanced methods are now available for conformally wrapping planar, silicon-based electronics circuits onto complex, curvilinear surfaces. Here, buckling physics of circuits configured into mesh geometries consisting of silicon islands interconnected by narrow ribbons leads to out of plane displacements across different parts of the curvilinear surface, in a way that accommodates strains associated with wrapping. The mechanisms for different buckling patterns are identified in this paper. A simple and robust method is established *via* the following steps to predict the buckling patterns of interconnect bridges for arbitrarily axisymmetric curvilinear surfaces: *step 1*, obtain analytically the strain distribution on the curvilinear surface; *step 2*, use the strain distribution from step 1 to determine the buckling patterns of interconnect bridges along different directions and at different locations on the curvilinear surface; and *step 3*, use the strain distribution from step 1 and buckling pattern from step 2 to obtain analytically the maximum strains in interconnect bridges and device islands. This method is useful to the design and optimization of curvilinear electronics against mechanical and electrical failure.

Downloaded by University of Illinois - Urbana on 02 November 2010
Published on 06 October 2010 on http://pubs.rsc.org | doi:10.1039/C0SM00579G

I. Introduction

Advanced strategies and procedures have been recently introduced that allow well-developed, 2D planar electronic circuits to be wrapped conformally onto complex, curvilinear surfaces.[1] These techniques enable integration of conventional silicon-based electronics on many envisioned systems of the future, for applications such as health monitoring systems on soft, curvilinear surfaces of living organisms (*e.g.*, brain and heart). Fig. 1 schematically illustrates the following steps for using compressible circuit mesh structures (consisting of arrays of islands interconnected by narrow strips of polyimide) and elastomeric transfer elements to wrap conformally curvilinear objects with complex shapes, such as the conical surface shown here. The processes include:

(A) First, a transfer element is fabricated in an elastomer such as poly(dimethylsiloxane) (PDMS) by double casting and thermal curing against the target object to be wrapped.

(B) The resulting element is radially stretched to form a flat drumhead membrane (see top right frame).

(C) The flat drumhead contacts a prefabricated circuit with an ultrathin mesh geometry in a planar configuration on a silicon wafer and then is peeled back to lift the circuit onto the membrane.

(D) The tension is relaxed to geometrically transform the transfer element and the circuit on its surface into the shape of the target object. During this process, the interconnect bridges of the mesh buckle to adopt non-coplanar arch shapes, which accommodate the compressive forces in a way that avoids significant strains in the circuit.

(E) Finally, the target object is coated with a thin layer of adhesive and the non-coplanar circuit mesh is transferred onto its surface.

Similar to Euler buckling of a beam, buckling of interconnect bridges on a hemispherical surface always yields arch shapes in

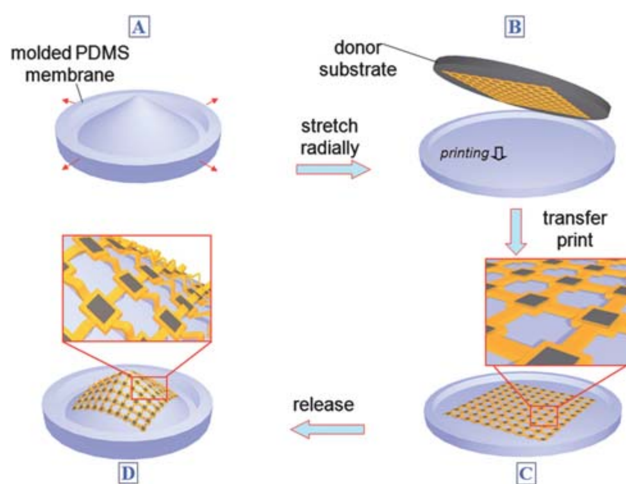

Fig. 1 Schematic illustration on using compressible circuit mesh structures and elastomeric transfer element to wrap conformally curvilinear object.

[a]Department of Mechanical Engineering, Northwestern University, Evanston, IL, 60208, USA. E-mail: y-huang@northwestern.edu
[b]Department of Materials Science and Engineering, University of Illinois, Urbana, IL, 61801, USA. E-mail: jrogers@uiuc.edu
[c]Department of Mechanical and Aerospace Engineering, University of Miami, Coral Gables, FL, 33146, USA
[d]Department of Materials Science and Engineering, Gwangju Institute of Science and Technology, Gwangju, 500-712, Korea
[e]Department of Engineering Mechanics, Tsinghua University, Beijing, 100084, China
[f]Department of Civil and Environmental Engineering, Northwestern University, Evanston, IL, 60208, USA
[g]Department of Mechanical Science and Engineering, Department of Electrical and Computer Engineering, Department of Chemistry, and Frederick Seitz Materials Research Laboratory, University of Illinois, Urbana, IL, 61801, USA

† This paper is part of a *Soft Matter* themed issue on The Physics of Buckling. Guest editor: Alfred Crosby.

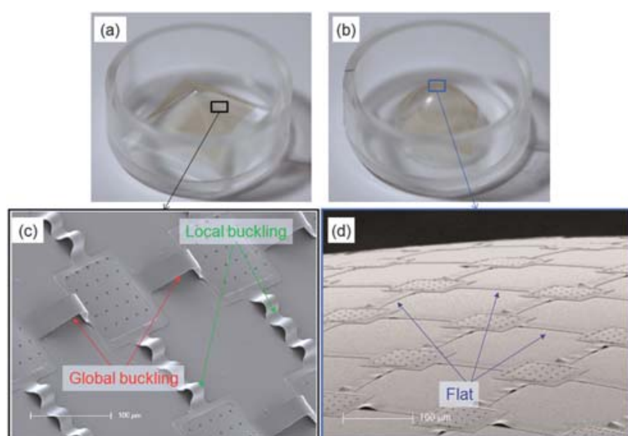

Fig. 2 Experimentally observed different buckling patterns of interconnect bridges in different areas of various shapes of curvilinear surfaces.

the interconnects,[2–4] which is referred to as *global buckling* in the present study. Buckling of interconnect bridges on a more complex shape, such as a pyramid (Fig. 2a), however, results in different patterns; each interconnect bridge along the circumferential direction buckles to a single arch (*i.e.*, global buckling), but each bridge along the meridional direction buckles to multiple, small arches, which is referred to as *local buckling* (Fig. 2c) in this study. The interconnect bridges around the top of a parabola (Fig. 2b and d) do not buckle at all, *i.e.*, *no buckling*. These different buckling modes lead to different strains in the circuit mesh structures.

Vella *et al.*[5] and others[6–8] have investigated the delamination of a stiff film from a compliant substrate from a fracture mechanics point of view (energy release rate). The present study focuses on the buckling-driven delamination[9–13] pertinent to the experiments in Fig. 1 and 2, for which the delamination is driven by buckling of the stiff film such that the buckling condition must be satisfied prior to any delamination.[13] The present study investigates the mechanisms for the aforementioned different buckling modes, establishes a simple criterion for predicting buckling patterns, and obtains strains in the buckled interconnects and flat device islands, on arbitrarily axisymmetric curvilinear objects. For an arbitrary (axisymmetric) elastomeric transfer element stretched to flat (step B above), Section II gives analytically the strain distribution in both circumferential and meridional directions. A simple, analytic criterion separating different buckling modes (*global buckling*, *local buckling*, and *no buckling*) is established in Section III, which shows that the strain distribution in the transfer element obtained in Section II determines the buckling patterns upon relaxation of tension observed in experiments (step D above). Finally, based on the strain distribution from Section II and buckling patterns from Section III, the strain in the circuit mesh structure wrapped onto the curvilinear object is determined analytically in Section IV.

II. Strain distribution in stretched elastomeric transfer elements

The mean and Gaussian curvatures[14,15] are widely adapted to characterize curvilinear surfaces, such as the deformation of shells.[16–18] Such an approach, however, usually involves the numerical method, and cannot lead to simple, analytical solutions. For the special case of an axisymmetric transfer element stretched to flat, a simple, analytic model is established in this section, and is verified by the finite element analysis.

Fig. 3 illustrates the mechanics model for the processes in Fig. 1 to integrate coplanar circuits onto a curvilinear target object. The general strategy represents an extension of the model for hemispherical target object[4,19] to arbitrarily axisymmetric objects. Such an approach has been validated by the finite element method,[4,19] for hemispherical objects. An elastomeric transfer element has the surface geometry of the object, and is characterized by $R = R(z)$ in the cylindrical coordinates (R, z), where $z \in (0, z_{max})$ (step A). This transfer element is radially stretched to a (nearly) flat shape (step $\overline{AB}$), and then further stretched to a plate of radius r_B (step B). A circuit mesh is then transfer printed[20–22] onto the transfer element in its tensioned, planar shape (step C). Releasing the radial tension causes the transfer element to relax back to a new shape $R'(z')$ with height z'_{max} to be determined (step D), where (R', z') corresponds to the deformed position of original point (R, z), through an intermediate step $\overline{CD}$ that gives a (nearly) flat shape (similar to step $\overline{AB}$).

Finite element analysis[4,19] has shown that, from step A to step $\overline{AB}$, the transfer element is mainly stretched in the circumferential direction, and the strain in the meridional direction is

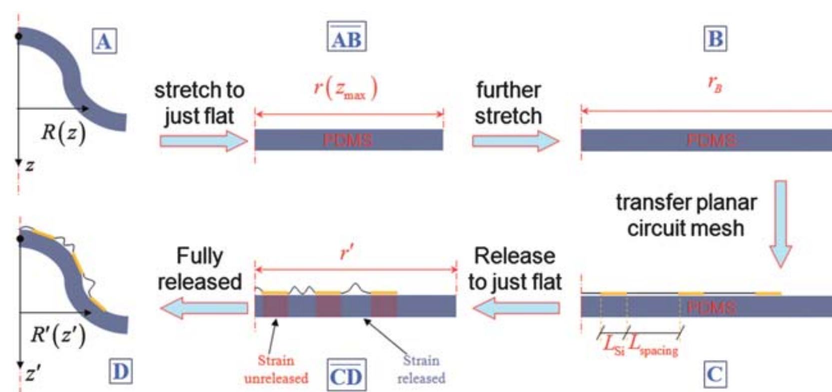

Fig. 3 Schematic diagrams of the mechanics model for transferring compressible circuit mesh structures from planar arrays onto an arbitrarily axisymmetric curvilinear elastomeric transfer element.

 This journal is © The Royal Society of Chemistry 2010

Downloaded by University of Illinois - Urbana on 02 November 2010
Published on 06 October 2010 on http://pubs.rsc.org | doi:10.1039/C0SM00579G

negligibly small, $\varepsilon_{\text{meridional}} \approx 0$. Therefore, a ring at the height z ($0 \le z \le z_{\max}$) in step A becomes a ring of the following radius in step $\overline{\text{AB}}$

$$r(z) = \int_0^z \sqrt{1 + \left[\frac{dR(y)}{dy}\right]^2} dy, \quad (1)$$

which equals the arc length from 0 to z in step A. The circular plate of radius $r(z_{\max})$ in step $\overline{\text{AB}}$ is then further stretched to radius of r_B in step B, which imposes uniform strains in both meridional and circumferential directions. Therefore, the strains on the surface of elastomeric transfer element are given by:

$$\varepsilon_{\text{circumferential}} \approx \frac{r_B}{r(z_{\max})} \frac{r(z)}{R(z)} - 1, \quad (2)$$

$$\varepsilon_{\text{meridional}} \approx \frac{r_B}{r(z_{\max})} - 1. \quad (3)$$

Fig. 4 shows that the distribution of circumferential strain given by eqn (2) agrees well with the finite element analysis for the parabolic elastomeric transfer element in Fig. 2b, which has the shape $R(z) = \sqrt{7.58z}$ for $0 \le z \le 6.9$ (unit: mm) and thickness of 0.3 mm. An inset in Fig. 4 shows the initial mesh of the parabola and the deformed mesh when the transfer element is stretched to flat at $r_B = 10.3$ mm as in experiments. The meridional strain given by eqn (3) is very small; finite element analysis also gives small meridional strain (~2%). Therefore, the analytical expressions (2) and (3) provide good estimates of strains in stretched elastomeric transfer elements.

The circuit mesh is transferred to the surface of elastomeric transfer element in step C. Releasing the tension leads first to a (nearly) flat plate with radius r' in the intermediate step $\overline{\text{CD}}$, and then to the curvilinear shape in step D. From step C to $\overline{\text{CD}}$, the stretch in the elastomer is released except for that beneath the device islands since the device islands (Young's modulus ≈ 130 GPa for silicon[23]) are much stiffer than the elastomer (Young's modulus ≈ 2 MPa for PDMS[24]). Therefore, the size of device islands L_{Si} remains unchanged, which gives their area fraction $f = \frac{NL_{Si}^2}{\pi r_B^2}$, where N is the number of device islands on the elastomer in step C. The average fractions of device islands and spacings along any direction are f and $1 - f$, respectively, such that the radius of the circular plate in the intermediate step $\overline{\text{CD}}$ is $r' = fr_B + (1 - f)r(z_{\max})$. Releasing the tension from step $\overline{\text{CD}}$ to D is mainly in the circumferential direction. The negligible strain in the meridional direction gives

$$\int_0^{z'} \sqrt{1 + \left[\frac{dR'(y)}{dy}\right]^2} dy = r' \frac{r(z)}{r(z_{\max})} = \left[\frac{fr_B}{r(z_{\max})} + (1 - f)\right] r(z). \quad (4)$$

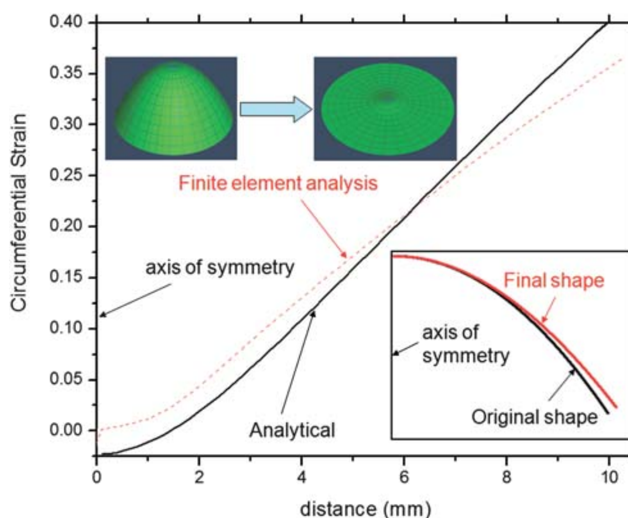

Fig. 4 Distribution of circumferential strain for a parabolic elastomeric transfer element stretched to flat. The insets show the finite element meshes for the initial and stretched configurations, as well as the initial and final shapes of the transfer element after the circuits are printed.

The above analysis can also be applied to the circumferential direction. The perimeter $2\pi R'(z')$ of the deformed elastomeric transfer element at any height $z' \in (0, z'_{\max})$ in step D consists of the unreleased part $2\pi f r_B \frac{r(z)}{r(z_{\max})}$ underneath the device islands and the released part $(1 - f) \times 2\pi R(z)$. This gives

$$R'(z') = fr_B \frac{r(z)}{r(z_{\max})} + (1 - f)R(z). \quad (5)$$

The function R' can be eliminated from eqn (4) and (5) to give z' as a function of z,

$$z' = \int_0^z \sqrt{(1-f)^2 + 2\frac{(1-f)fr_B}{r(z_{\max})}\sqrt{1 + \left[\frac{dR(y)}{dy}\right]^2}\left\{\sqrt{1 + \left[\frac{dR(y)}{dy}\right]^2} - \frac{dR(y)}{dy}\right\}} dy. \quad (6)$$

The maximum height $z'_{\max}$ of the deformed shape is obtained by replacing z in the above equation with $z_{\max}$. The substitution of eqn (6) into (5) then gives the function R' for any given (R, z). For $N = 3025$ (55 × 55) square device islands of $L_{Si} = 0.1$ mm on the parabolic transfer element in Fig. 2b, the area fraction is $f = 0.0916$ for the stretch $r_B = 10.3$ mm in experiments. The inset in Fig. 4 shows that the new shape $R'(z')$ is close to the initial parabolic shape $R(z)$ because of the small area fraction f. The maximum height is reduced from $z_{\max} = 6.9$ mm to $z'_{\max} = 6.64$ mm. This small change in shape helps the conformal wrapping of deformed transfer element onto the target object. As the area fraction (*i.e.*, fill factor) f increases (*e.g.*, $f > 50\%$), the final shape will be very different from the initial one.

III. Buckling of interconnect bridges

Relaxation of the stretched elastomeric transfer element, with the circuit mesh structure transfer printed on its surface, leads to buckling of interconnect bridges. For each interconnect bridge,

Downloaded by University of Illinois - Urbana on 02 November 2010
Published on 06 October 2010 on http://pubs.rsc.org | doi:10.1039/C0SM00579G

View Online

the strain given in Section II becomes a compressive strain upon relaxation of the stretch, with the ability to induce buckling of the interconnect bridges.

Ko *et al.*[1] analyzed different buckling modes (global buckling, local buckling, and no buckling) of interconnect bridges. Their analysis, summarized in the following, is combined with the strain distribution in Section II to determine the buckling of interconnect bridges on complex curvilinear objects.

Let L and h denote the length and thickness of interconnect bridges, E the Young's modulus, and γ the work of adhesion between the bridge and the transfer element. The interconnect bridge is subjected to the axial compressive strain ε (<0). Prior to buckling the bridge remains flat such that the total potential energy U_{flat} consists of the membrane energy $U_{\text{membrane}} = \frac{1}{2}EhL|\varepsilon|^2$ and adhesion energy $U_{\text{adhesion}} = -\gamma L$ of the interface, *i.e.*, $U_{\text{flat}} = \frac{1}{2}EhL|\varepsilon|^2 - \gamma L$.

For global buckling, the interconnect bridge buckles to an arch shape. The corresponding out-of-plane displacement $w = \frac{A}{2}\left(1 + \cos\frac{2\pi x}{L}\right)$ satisfies the condition of vanishing displacement and slope at the two ends ($x = \pm L/2$), where A is the buckle amplitude to be determined. In this configuration, there is no adhesion energy, and the total potential energy U_{global} consists of the membrane energy $U_{\text{membrane}} = \frac{1}{2}EhL\left(\frac{\pi^2 A^2}{4L^2} - |\varepsilon|\right)^2$ and bending energy $U_{\text{bending}} = \frac{\pi^4 Eh^3 A^2}{12L^3}$. Energy minimization gives the buckle amplitude $A = \frac{2L}{\pi}\sqrt{|\varepsilon| - \varepsilon_c}$, where $\varepsilon_c = \frac{\pi^2 h^2}{3L^2}$ is the Euler buckling strain. This result gives the total energy for global buckling $U_{\text{global}} = EhL\varepsilon_c\left(|\varepsilon| - \frac{\varepsilon_c}{2}\right)$, which must be less than U_{flat} for global buckling to occur. This equation then gives the critical strain for transition from flat to global buckling as:

$$\left(\frac{|\varepsilon|}{\varepsilon_c}\right)_{\text{flat-global}} = 1 + \sqrt{\frac{2\gamma}{Eh\varepsilon_c^2}}. \tag{7}$$

For local buckling, the interconnect bridge buckles to small arches with amplitude a and wavelength l to be determined. The total potential energy U_{local} consists of the membrane energy $U_{\text{membrane}} = \frac{1}{2}EhL\left(\frac{\pi^2 a^2}{4lL} - |\varepsilon|\right)^2$, bending energy $U_{\text{bending}} = \frac{\pi^4 Eh^3 a^2}{12 l^3}$, and adhesion energy $U_{\text{adhesion}} = -\gamma(L - l)$ of the interface. Energy minimization with respect to a and l gives $a = \frac{2l}{\pi}\sqrt{\left(|\varepsilon| - \frac{\pi^2 h^2}{3l^2}\right)\frac{L}{l}}$, and the following algebraic equation to determine l:

$$\frac{\pi^2 h^3}{3l^3}\left(\frac{\pi^2 h^2}{3l^2} - |\varepsilon|\right) + \frac{\gamma}{2EL} = 0. \tag{8}$$

Its solution takes the form $\frac{l}{h} = g\left(|\varepsilon|, \frac{\gamma}{EL}\right)$, where the non-dimensional function g increases with $|\varepsilon|$, but decreases as $\frac{\gamma}{EL}$ increases. The total energy for local buckling is then obtained as $U_{\text{local}} = \frac{\pi^2 EhL}{3g^2(|\varepsilon|, \frac{\gamma}{EL})}\left[|\varepsilon| - \frac{\pi^2}{6g^2(|\varepsilon|, \frac{\gamma}{EL})}\right] - \gamma L\left[1 - \frac{h}{L}g\left(|\varepsilon|, \frac{\gamma}{EL}\right)\right]$, which must be less than U_{flat} for local buckling to occur. This result gives the critical strain for transition from flat to local buckling,

$$\left(\frac{|\varepsilon|}{\varepsilon_c}\right)_{\text{flat-local}} = 5\left(\frac{\gamma}{8Eh\varepsilon_c^2}\right)^{2/5}. \tag{9}$$

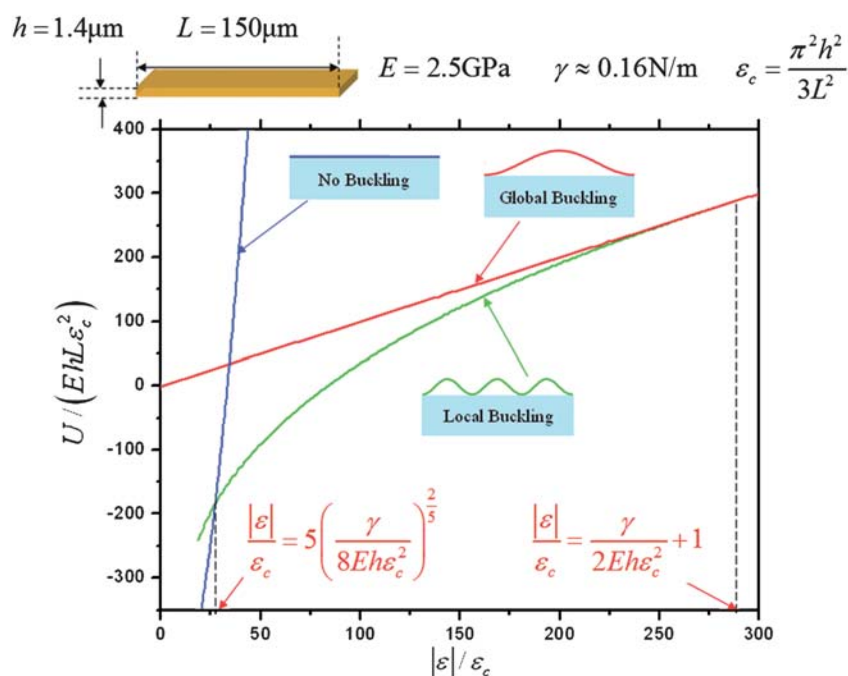

Fig. 5 Comparison of the energy curves for the global, local and no buckling modes.

 This journal is © The Royal Society of Chemistry 2010

Published on 06 October 2010 on http://pubs.rsc.org | doi:10.1039/C0SM00579G
Downloaded by University of Illinois - Urbana on 02 November 2010

View Online

Downloaded by University of Illinois - Urbana on 02 November 2010
Published on 06 October 2010 on http://pubs.rsc.org | doi:10.1039/C0SM00579G

For weak adhesion $\frac{\gamma}{8Eh\varepsilon_c^2}\leq 1$, the critical strain in eqn (9) is larger than that in eqn (7) such that global buckling occurs, and it can be shown that it never transitions to local buckling as the compressive strain increases. For relatively strong adhesion $\frac{\gamma}{8Eh\varepsilon_c^2}>1$, the critical strain in eqn (9) is smaller than that in eqn (7) such that local buckling occurs first. As the compressive strain $|\varepsilon|$ increases, global buckling occurs when its energy U_{global} becomes less than U_{local}, which gives the critical strain for the transition from local to global buckling as

$$\left(\frac{|\varepsilon|}{\varepsilon_c}\right)_{\text{local-global}} = 1 + \frac{\gamma}{2Eh\varepsilon_c^2}. \tag{10}$$

This result is illustrated in Fig. 5, which shows the normalized total potential energy for no buckling, local buckling and global buckling *versus* the normalized compressive strain $\frac{|\varepsilon|}{\varepsilon_c}$. The work of adhesion $\gamma = 0.16$ J m^{-2} between PDMS[22,25,26] and the polyimide interconnects ($E = 2.5$ GPa, $h = 1.4$ μm, and $L = 150$ μm) corresponds to strong adhesion because $\frac{\gamma}{8Eh\varepsilon_c^2} = 70$□1. Below the critical strain for local buckling 0.78% [eqn (9)], the total potential energy for no buckling is the lowest such that the interconnect bridge remains flat. This critical strain 0.78% is much (27 times) larger than the Euler buckling strain $\varepsilon_c = 0.029\%$ due to strong adhesion. Local buckling becomes the prevailing mode until the compressive strain reaches 8.0% [eqn (10)], at which global buckling gives the lowest energy. The critical strains, 0.78% and 8.0% for local and global buckling, respectively, have been confirmed by experiments of one-dimensional arrays of islands and interconnect bridges.[1]

Table 1 shows the range of compressive strain and work of adhesion for the different buckling modes (*e.g.*, global, local, and no buckling). For weak adhesion $\frac{\gamma}{8Eh\varepsilon_c^2}\leq 1$, there is never local buckling, and global buckling occurs once the compressive strain reaches $\varepsilon_c + \sqrt{\frac{2\gamma}{Eh}}$. For relatively strong adhesion $\frac{\gamma}{8Eh\varepsilon_c^2}>1$, local buckling occurs once the compressive strain reaches $5\left(\frac{\gamma\sqrt{\varepsilon_c}}{8Eh}\right)^{2/5}$, which is followed by global buckling once the compressive strain reaches $\varepsilon_c + \frac{\gamma}{2Eh\varepsilon_c}$.

Table 1 Critical compressive strains for local and global buckling

	Weak adhesion $\frac{\gamma}{8Eh\varepsilon_c^2}\leq 1$	Strong adhesion $\frac{\gamma}{8Eh\varepsilon_c^2}>1$
No buckling	$\lvert\varepsilon\rvert<\varepsilon_c + \sqrt{\frac{2\gamma}{Eh}}$	$\lvert\varepsilon\rvert<5\left(\frac{\gamma\sqrt{\varepsilon_c}}{8Eh}\right)^{2/5}$
Local buckling		$5\left(\frac{\gamma\sqrt{\varepsilon_c}}{8Eh}\right)^{2/5}\leq\lvert\varepsilon\rvert\leq\varepsilon_c + \frac{\gamma}{2Eh\varepsilon_c}$
Global buckling	$\lvert\varepsilon\rvert\geq\varepsilon_c + \sqrt{\frac{2\gamma}{Eh}}$	$\lvert\varepsilon\rvert>\varepsilon_c + \frac{\gamma}{2Eh\varepsilon_c}$

The results in Table 1, together with the strain distribution in Section II, provide a simple and robust way to determine the buckling patterns of interconnect bridges over different parts of curvilinear substrates, according to the following:

(1) use eqn (2) and (3) (or the finite element method) to determine the strain distribution along the meridional and circumferential directions on the curvilinear substrates;

(2) predict the buckling pattern (no buckling, local and global buckling) based on the above strain distribution and the criterion in Table 1; and

(3) use eqn (5) and (6) (or the finite element method) to identify the location of interconnect bridges on the new shape of relaxed elastomeric transfer element.

As an example to illustrate the above approach, Fig. 6a shows the strain distribution in the circumferential direction for the parabolic elastomeric transfer element in Fig. 2b (also Fig. 4) stretched to $r_B = 10.3$ mm. The contour values are set such that

(1) red color is for the compressive strain larger than 8%, which predicts global buckling;

(2) blue color is for the compressive strain smaller than 1% (including tensile strain), which predicts no buckling and therefore flat interconnects; and

(3) all other colors are for the compressive strain between 1% and 8%, which predicts local buckling.

The predicted buckling patterns based on the strain distribution agree well with the experiment in Fig. 6b for the parabolic transfer element shown. For example, Fig. 6c clearly shows global buckling along the circumferential direction away from the peak of parabola, which is consistent with the red color in Fig. 6a. Fig. 6d indicates no buckling around the peak, which is consistent with the blue color in Fig. 6a. The strain in the meridional direction (not shown in Fig. 6) is always small, which is consistent with local buckling away from the peak (Fig. 6c) or no buckling around the peak (Fig. 6d). The above approach also agrees well with experiments for many other complex shapes, such as pyramid, cone or even golf ball shapes.[1]

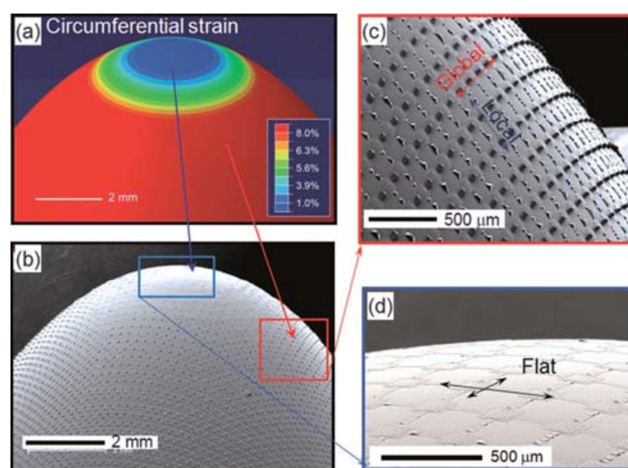

Fig. 6 (a) Distribution of circumferential strain for a parabolic elastomeric transfer element given by the mechanics model. (b–d) Buckling patterns observed in experiments.

View Online

Downloaded by University of Illinois - Urbana on 02 November 2010
Published on 06 October 2010 on http://pubs.rsc.org | doi:10.1039/C0SM00579G

IV. Maximum strain in the circuit mesh

Based on the strain distribution from Section II and buckling patterns from Section III, the maximum strain in the circuit mesh on the deformed curvilinear surface (step D in Fig. 1) is obtained analytically in this section. Even for a large compressive strain ε on the curvilinear substrate, the strain in the circuit mesh is still very small because the interconnect bridges buckle to accommodate the compression. Both analytical and finite element models are developed to determine the strain in the island-interconnect structure of circuit mesh. The interconnect bridges have the length L, thickness h, and Young's modulus E. The device islands consist of two layers of different materials—silicon (thickness h_{Si} and plane-strain modulus $\bar{E}_{Si}$) and polyimide (thickness h_{PI} and plane-strain modulus $\bar{E}_{PI}$). For an interconnect bridge subject to a large compressive strain ε (<0), global buckling will occur, and the maximum strain in the interconnect bridge is given by:[2]

$$\varepsilon_{\text{interconnect}}^{\max} = \frac{2\pi h}{L}\sqrt{|\varepsilon| - \varepsilon_c}, \tag{11}$$

where $\varepsilon_c = \dfrac{\pi^2 h^2}{3L^2}$ is the Euler buckling strain. The device island is modeled as a composite plate of silicon and polyimide, which has an equivalent bending stiffness $\overline{EI}_{\text{island}}$ and distance h_{NA} between the neutral axis and top surface of the island. The device island, sitting on the PDMS substrate, is subject to compression and bending resulting from buckling of interconnect bridges. The maximum strain in silicon is obtained as:[2]

$$\varepsilon_{\text{island}}^{\max} = \frac{\pi E h^3 h_{NA}}{3\overline{EI}_{\text{island}} L}\sqrt{\frac{|\varepsilon|}{1+|\varepsilon|}}, \tag{12}$$

For silicon and polyimide having the comparable thickness ($h_{Si} \approx h_{PI}$) but very different moduli ($E_{Si} \gg E_{PI}$) as in experiments, h_{NA} and $\overline{EI}_{\text{island}}$ are given by:

$$h_{NA} \approx \frac{h_{Si}}{2}, \quad \overline{EI}_{\text{island}} \approx 13\frac{\bar{E}_{PI} + \bar{E}_{Si}}{96}(h_{Si} + h_{PI})^3. \tag{13}$$

This result gives the maximum strain in silicon in eqn (12)

$$\varepsilon_{\text{island}}^{\max} = \frac{16\pi E h^3 h_{Si}}{(13\bar{E}_{PI} + \bar{E}_{Si})(h_{Si} + h_{PI})^3 L}\sqrt{\frac{|\varepsilon|}{1+|\varepsilon|}}. \tag{14}$$

The finite element method is used to validate the maximum strains in eqn (11) and (14). The computational model consists of one half of the device island and one half of the interconnect bridge due to symmetry. The polyimide interconnect bridge has Young's modulus $E = 2.5$ GPa, thickness $h = 1.4$ μm, and half-length $L/2 = 75$ μm; the island is made of silicon (plane-strain modulus $\bar{E}_{Si} = 140$ GPa and thickness $h_{Si} = 700$ nm) and polyimide (plane-strain modulus $\bar{E}_{PI} = 2.83$ GPa and thickness $h_{PI} = 900$ nm), and has the half-length 50 μm. For the stretch of elastomeric transfer element to $r_B = 10.3$ mm, as in experiments, the maximum strain reaches 34.0% at the outermost point of the circuit mesh (9.62 mm from the center). The relaxation of stretch then imposes compression on the interconnect (and island). The eigenvalues and eigenmodes of the system are first obtained in the finite element analysis, and then used in the post-buckling analysis. The deformation and strain distribution of the circuit mesh are shown in Fig. 7b–d, while Fig. 7a gives the experimental image of buckled shape. The maximum strain in the interconnect bridge is 3.2% (Fig. 7d), which is very close to 3.4% given by eqn (11). The maximum strain in silicon is 0.16% (Fig. 7c), which is also close to 0.13% given by eqn (14). These strains are much smaller respectively than the corresponding fracture strains of polyimide (~7%) and silicon (~1%).[1] Therefore, eqn (11) and (14) provide simple and robust ways to estimate the strains in the circuits on curvilinear surfaces.

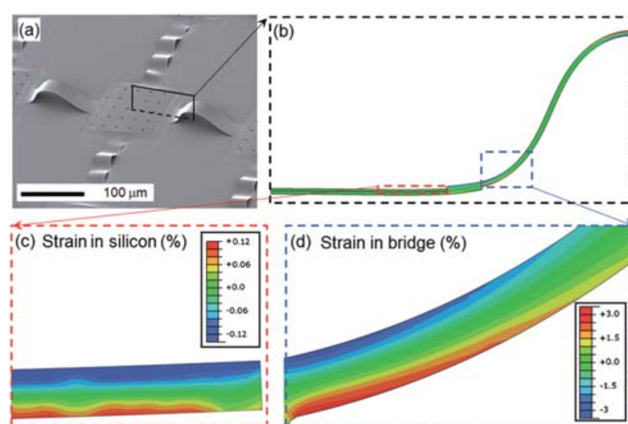

Fig. 7 Buckled interconnect bridges and deformed device islands observed in experiments (a) and finite element analysis (b). The strain distributions in silicon part of the island and in the interconnect bridge are shown in (c) and (d).

V. Concluding remarks

An analytical model is established for transfer printing planar, silicon-based electronics circuits onto complex, curvilinear surfaces. The compressible circuits consist of silicon islands interconnected by narrow polyimide strips, which display different buckling patterns along the circumferential and meridional directions and over different parts of the curvilinear surface. It is shown that the adhesion between interconnect bridges and transfer elements, together with the compressive strain, control the buckling pattern. The strain distribution on the curvilinear surface is obtained analytically, based on which the buckling patterns agree well with the experiments. The maximum strains in the interconnect bridges and device islands are then obtain analytically, and they agree well with the finite element analysis. These outcomes provide a simple and robust method for the design and optimization of circuit mesh structure for any curvilinear surface.

Acknowledgements

The authors acknowledge support from NSF Grant No. DMI-0328162 and ECCS-0824129, and DOE, Division of Materials Sciences Grant No. DE-FG02-07ER46453. J. Song acknowledges the supports from the Provost Award (University of Miami), the Ralph E. Powe Junior Faculty Enhancement Award (ORAU) and NSF Grant No. OISE1043161.

This journal is © The Royal Society of Chemistry 2010

View Online

Downloaded by University of Illinois - Urbana on 02 November 2010
Published on 06 October 2010 on http://pubs.rsc.org | doi:10.1039/C0SM00579G

References

1 H. C. Ko, G. Shin, S. Wang, M. P. Stoykovich, J. W. Lee, D.-H. Kim, J. S. Ha, Y. Huang, K.-C. Hwang and J. A. Rogers, *Small*, 2009, **5**, 2703–2709.
2 J. Song, Y. Huang, J. Xiao, S. Wang, K.-C. Hwang, H. C. Ko, D.-H. Kim, M. P. Stoykovich and J. A. Rogers, *J. Appl. Phys.*, 2009, **105**, 123516.
3 G. Shin, I. Jung, V. Malyarchuk, J. Song, S. Wang, H. C. Ko, Y. Huang, J. S. Ha and J. A. Rogers, *Small*, 2010, **6**, 851–856.
4 H. C. Ko, M. P. Stoykovich, J. Song, V. Malyarchuk, W. M. Choi, C.-J. Yu, J. B. Geddes, J. Xiao, S. Wang, Y. Huang and J. A. Rogers, *Nature*, 2008, **454**, 748–753.
5 D. Vella, J. Bico, A. Boudaoud, B. Roman and P. M. Reis, *Proc. Natl. Acad. Sci. U. S. A.*, 2009, **106**, 10901–10906.
6 B. Cotterell and Z. Chen, *Int. J. Fract.*, 2000, **104**, 169–179.
7 G. Gioia and M. Ortiz, in *Advances in Applied Mechanics*, ed. W. H. John and Y. W. Theodore, Elsevier, 1997, vol. 33, pp. 119–192.
8 K. Kendall, *Nature*, 1976, **261**, 35–36.
9 N. R. Moody, E. D. Reedy, E. Corona, D. P. Adams, M. S. Kennedy, M. J. Cordill and D. F. Bahr, *EPJ Web Conf.*, 2010, **6**, 40006.
10 J. W. Hutchinson, *J. Mech. Phys. Solids*, 2001, **49**, 1847–1864.
11 M. D. Thouless, J. W. Hutchinson and E. G. Liniger, *Acta Metall. Mater.*, 1992, **40**, 2639–2649.
12 J. W. Hutchinson, M. D. Thouless and E. G. Liniger, *Acta Metall. Mater.*, 1992, **40**, 295–308.
13 A. G. Evans and J. W. Hutchinson, *Int. J. Solids Struct.*, 1984, **20**, 455–466.
14 H. Yamauchi, S. Gumhold, R. Zayer and H.-P. Seidel, *Vis. Comput.*, 2005, **21**, 659–668.
15 H. T. Jung, S. Y. Lee, E. W. Kaler, B. Coldren and J. A. Zasadzinski, *Proc. Natl. Acad. Sci. U. S. A.*, 2002, **99**, 15318–15322.
16 M. Marder, R. D. Deegan and E. Sharon, *Phys. Today*, 2007, **60**, 33–38.
17 H. Stumpf and J. Makowski, *Acta Mech. Sin.*, 1987, **65**, 153–168.
18 L. A. Taber, *Int. J. Nonlinear Mech.*, 1985, **20**, 27–39.
19 S. Wang, J. Xiao, I. Jung, J. Song, H. C. Ko, M. P. Stoykovich, Y. Huang, K.-C. Hwang and J. A. Rogers, *Appl. Phys. Lett.*, 2009, **95**, 181912.
20 X. Feng, M. A. Meitl, A. M. Bowen, Y. Huang, R. G. Nuzzo and J. A. Rogers, *Langmuir*, 2007, **23**, 12555–12560.
21 M. A. Meitl, Z. T. Zhu, V. Kumar, K. J. Lee, X. Feng, Y. Y. Huang, I. Adesida, R. G. Nuzzo and J. A. Rogers, *Nat. Mater.*, 2006, **5**, 33–38.
22 Y. G. Y. Huang, W. X. Zhou, K. J. Hsia, E. Menard, J. U. Park, J. A. Rogers and A. G. Alleyne, *Langmuir*, 2005, **21**, 8058–8068.
23 R. Hull, *Properties of Crystalline Silicon*, INSPEC, London, 1999.
24 E. A. Wilder, S. Guo, S. Lin-Gibson, M. J. Fasolka and C. M. Stafford, *Macromolecules*, 2006, **39**, 5956–5956.
25 B. M. Z. Newby, M. K. Chaudhury and H. R. Brown, *Science*, 1995, **269**, 1407–1409.
26 M. K. Chaudhury and G. M. Whitesides, *Langmuir*, 1991, **7**, 1013–1025.